DRAFT VERSION MAY 10, 2020
Typeset using LATEX **twocolumn** style in AASTeX62

PTFO 8-8695: Two Stars, Two Signals, No Planet

L. G. BOUMA,[1] J. N. WINN,[1] G. R. RICKER,[2] R. VANDERSPEK,[2] D. W. LATHAM,[3] S. SEAGER,[2,4,5] J. M. JENKINS,[6] T. BARCLAY,[7,8] K. A. COLLINS,[3] J. P. DOTY,[9] D. LOUIE,[8] S. N. QUINN,[3] M. E. ROSE,[6] J. C. SMITH,[6,10] J. VILLASEÑOR,[2] AND B. WOHLER[6,10]

[1]*Department of Astrophysical Sciences, Princeton University, 4 Ivy Lane, Princeton, NJ 08540, USA*
[2]*Department of Physics and Kavli Institute for Astrophysics and Space Research, Massachusetts Institute of Technology, Cambridge, MA 02139, USA*
[3]*Center for Astrophysics | Harvard & Smithsonian, 60 Garden St, Cambridge, MA 02138, USA*
[4]*Department of Earth, Atmospheric and Planetary Sciences, Massachusetts Institute of Technology, Cambridge, MA 02139, USA*
[5]*Department of Aeronautics and Astronautics, MIT, 77 Massachusetts Avenue, Cambridge, MA 02139, USA*
[6]*NASA Ames Research Center, Moffett Field, CA 94035, USA*
[7]*NASA Goddard Space Flight Center, 8800 Greenbelt Road, Greenbelt, MD 20771, USA*
[8]*University of Maryland, Baltimore County, 1000 Hilltop Circle, Baltimore, MD 21250, USA*
[9]*Noqsi Aerospace Ltd., 15 Blanchard Avenue, Billerica, MA, 01821, USA*
[10]*SETI Institute, Mountain View, CA 94043, USA*

(Received May 10, 2020; Revised —; Accepted —)

ABSTRACT

PTFO 8-8695 (CVSO 30) is a star in the 7–10 million year old Orion-OB1a cluster that shows brightness dips that resemble planetary transits. While strong evidence against the planet hypothesis has already been provided, the possibility remains debated in the literature. To obtain further clues, we inspected data from the NASA *Transiting Exoplanet Survey Satellite* (TESS) and the ESA Gaia mission. The Gaia data show that PTFO 8-8695 is a photometric binary with respect to members of its kinematic group, and independently suggest that it is an astrometric binary. The TESS lightcurve shows two different photometric periods. The variability is dominated by a sinusoidal signal with a period of 11.98 hr, presumably caused by stellar rotation. Also present is a 10.76 hr signal consisting of a not-quite sinusoid interrupted by hour-long dips, the type of signal previously intepreted as planetary transits. The phase of the dips is nearly 180° away from the phase of the originally reported dips. As noted previously, this makes them difficult to explain as planetary transits. Instead, we believe that PTFO 8-8695 is a pair of young and rapidly rotating M dwarfs, one of which shows the same "transient-dipper" behavior that been seen in at least 5 other cases. The origin of these transient dips is still unknown but likely involves circumstellar material.

Keywords: Exoplanet evolution (491), Pre-main sequence stars (1290), Stellar ages (1581), Stellar rotation (1629), Variable stars (1761), Low mass stars (2050)

1. INTRODUCTION

We wish PTFO 8-8695b were a planet. It would be quite exceptional. It would be the youngest known hot Jupiter (van Eyken et al. 2012), orbiting a T Tauri star in the Orion-OB1a cluster. It would have the shortest orbital period (10.7 hours) of any hot Jupiter. With such a short period, it would probably be filling its Roche lobe, and actively losing mass to its host star. Not only that, but the rapidly-rotating host star is probably oblate enough to torque the planet's orbit into and out of the transiting configuration on a time scale of years (Barnes et al. 2013; Ciardi et al. 2015; Kamiaka et al. 2015).

Corresponding author: L. G. Bouma
luke@astro.princeton.edu

Another first would be the direct detection of Hα emission from the planet itself (Johns-Krull et al. 2016). In addition to the chromospheric Hα emisson, it seems that there is an additional Hα emission with radial velocity variations in phase with the planetary orbit. The average velocity width of the excess Hα emission is 87 km s^{-1}, and its equivalent width is 70-80% that of the stellar chromosphere (Johns-Krull et al. 2016). The proposed explanation is that the emission is from hot material flowing away from the planet (Johns-Krull et al. 2016).

However, the observed signals have some peculiarities that make the planet seem even more unusual, to the point that they cast into doubt the premise that PTFO 8-8695b is real. First, the transit-like brightness dips are about three times deeper in optical bandpasses (*e.g.*, g-band) than in the near-infrared (*e.g.*, z-band) (Onitsuka et al. 2017; Tanimoto et al. 2020). An ordinary atmosphere expected for a Jovian planet would not lead to such a strong color-dependence of the transits. Second, the planet does not seem to emit as much infrared radiation as would be expected for such a hot Jovian planet (Yu et al. 2015). Third, despite measurement attempts by multiple investigators, PTFO 8-8695b does not seem to show the Rossiter effect at the amplitude expected given the rapid stellar rotation and large planet size (Yu et al. 2015; Ciardi et al. 2015). Fourth, the phase of the dips within the overall period of photometric variability has changed drastically over the years since their initial discovery. To counter these objections, it has been proposed that the planet may be much smaller than Jupiter and that the dips are produced by dust clouds emitted from the planet (Tanimoto et al. 2020).

A separate issue is that the brightness dips change shape over many orbital cycles. This was initially explained by Barnes et al. (2013) as the natural effects of gravity darkening. However, Howarth (2016) argued that the necessary amplitude of gravity darkening is too large to be realistic, given the spectroscopically-determined rotation velocity. Additionally, as the gravity-darkened star precessed about its rotation axis, it would show photometric variability that has not been observed.

While the planetary interpetation clearly faces challenges, there is no completely satisfactory alternate explanation. High-latitude accretion hotspots might produce the observed Hα variability, but require fine-tuning to produce dips of the appropriate duration. Furthermore, PTFO 8-8695 does not have an infrared (IR) excess associated with the presence of dust at the inner edge of a primordial disk (*e.g.*, Yu et al. 2015, Figure 18). Low-latitude starspots, hot or cold, struggle to produce photometric features as short as some of the observed dips.

A relevant fact is that between 0.1% and 1% of rapidly rotating low-mass stars in $\mathcal{O}(10)$ Myr old associations show short-duration dips as part of their overall periodic variability (Rebull et al. 2018). The dips can persist over months, but their depths often vary, and sometimes change immediately after stellar flares. The explanation proposed by Stauffer et al. (2017) and David et al. (2017) to explain this novel class of variable stars is that a circumstellar cloud of gas is orbiting near the co-rotation radius. To this point, though, it has not been clear if this explanation applies to PTFO 8-8695, because the determination of the stellar rotation period has been somewhat ambiguous (van Eyken et al. 2012; Koen 2015; Raetz et al. 2016).

We begin in Section 2 by describing newly available observations from TESS (Ricker et al. 2015) and Gaia (Gaia Collaboration et al. 2018). The TESS lightcurve shows two different periodic signals, which we analyze in Section 3. The Gaia data, analyzed in Section 4, show that PTFO 8-8695 is a photometric binary, and suggest it is also an astrometric binary. We discuss the pieces of the puzzle in Section 5, and summarize the situation in Section 6. We comment on the study by Koen (2020) in postscript.

2. THE DATA

2.1. *TESS Observations*

PTFO 8-8695 [also known as CVSO 30; Briceño et al. 2005] was observed by TESS with Camera 1, CCD 1, from December 15, 2018 until January 6, 2019, during the sixth sector of science operations (Ricker et al. 2015). The star was designated TIC 264461976 in the TESS Input Catalog (Stassun et al. 2018, 2019). The pixel data for an 11×11 array surrounding PTFO 8-8695 were averaged into 2-minute stacks by the onboard computer. Each 2048$\times$2048 image from the CCD was also averaged into 30-minute stacks, and saved as a "full frame image" (FFI).

The 2-minute stacks for PTFO 8-8695 were reduced to lightcurves by the Science Processing Operations Center (SPOC) at NASA Ames (Jenkins et al. 2016). We mainly used the Presearch Data Conditioning (PDC) lightcurve. The PDC lightcurve aperture used pixels chosen to maximize the SNR of the total flux of the target (Smith et al. 2016). Non-astrophysical variability was removed by fitting out trends common to many stars (Smith et al. 2012; Stumpe et al. 2014).

As an independent check on the 2-minute SPOC lightcurve, we examined the lightcurve based upon 30-minute image stacks which was produced as part of the Cluster Difference Imaging Photometric Survey (CDIPS; Bouma et al. 2019). Our CDIPS lightcurve of choice used a circular aperture with radius 1 pixel.

To clean the data, we removed all points with non-zero quality flags, which indicate known problems (*e.g.*, Tenenbaum & Jenkins 2018). We also masked out the data from the first and last 6 hours of each orbit, since there are often systematic red noise in the photometry during those times. Both the CDIPS and PDC lightcurves showed a clear discontinuous jump in the last few days of orbit 20, which seemed likely to be an instrumental systematic effect. We correspondingly masked out the data with timestamps ranging from BJD 2458488.3 until the end of the orbit. The PDC lightcurve initially had 15,678 points. The quality-flag cut removed 854 points; masking the orbit edges removed an additional 716 points; and removing the data from the final few days of orbit 20 removed an additional 1079 points. After cleaning, 83% of the initial flux measurements remained.

We normalized the lightcurve by dividing out the median flux, and then opted to subtract 1.0 to set the median value to zero, which simplified subsequent interpretation. Many of these and subsequent processing steps were performed using `astrobase` (Bhatti et al. 2018).

2.2. *Gaia Observations*

2.2.1. *Astrometric measurements*

Between July 25, 2014 and May 23, 2016, Gaia measured about 300 billion centroid positions of 1.6 billion stars (Gaia Collaboration et al. 2016; Lindegren et al. 2018; Gaia Collaboration et al. 2018). In the Gaia second data release (DR2), these CCD observations were used to determine positions, proper motions, and parallaxes of the brighest 1.3 billion stars, including PTFO 8-8695 (Lindegren et al. 2018). For PTFO 8-8695, there were 121 "good" observations, *i.e.*, ob-

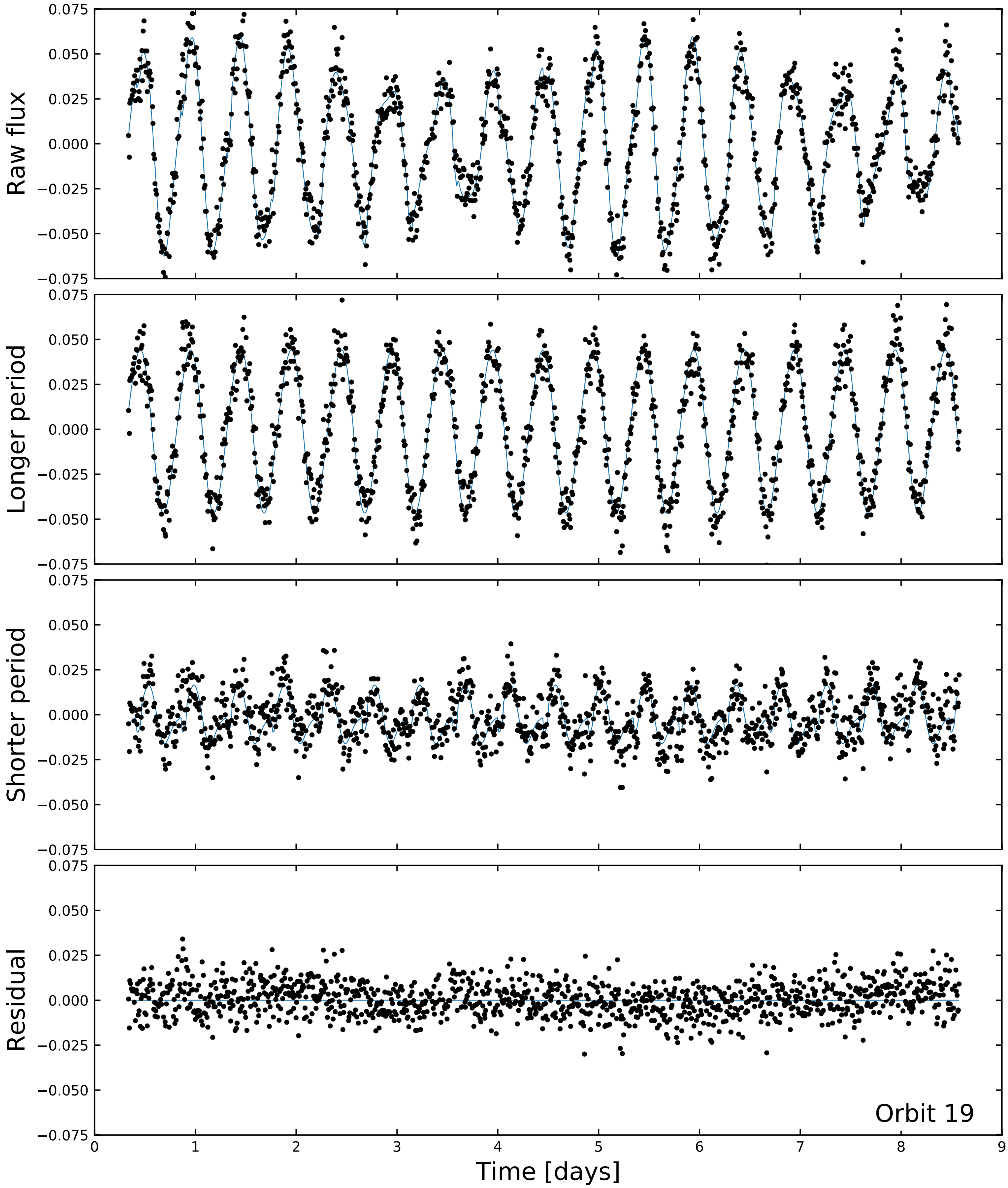

Figure 1. TESS lightcurve of PTFO 8-8695 (Sector 6, Orbit 19). *Top*: The "raw" (`PDCSAP` mean-subtracted) relative flux. The beat period of 4.48 days is visible by eye. The blue curve is a model including 2 harmonics at the longer period P_ℓ, plus 2 harmonics and a transit at the shorter period P_s. *Upper middle*: Longer-period signal, equal to the raw signal minus the shorter-period signal. *Lower middle*: Shorter-period signal, equal to the raw signal minus the longer-period signal. *Bottom*: residual relative flux. The data are binned from 2 to 10 minute cadence as a convenience for plotting and fitting.

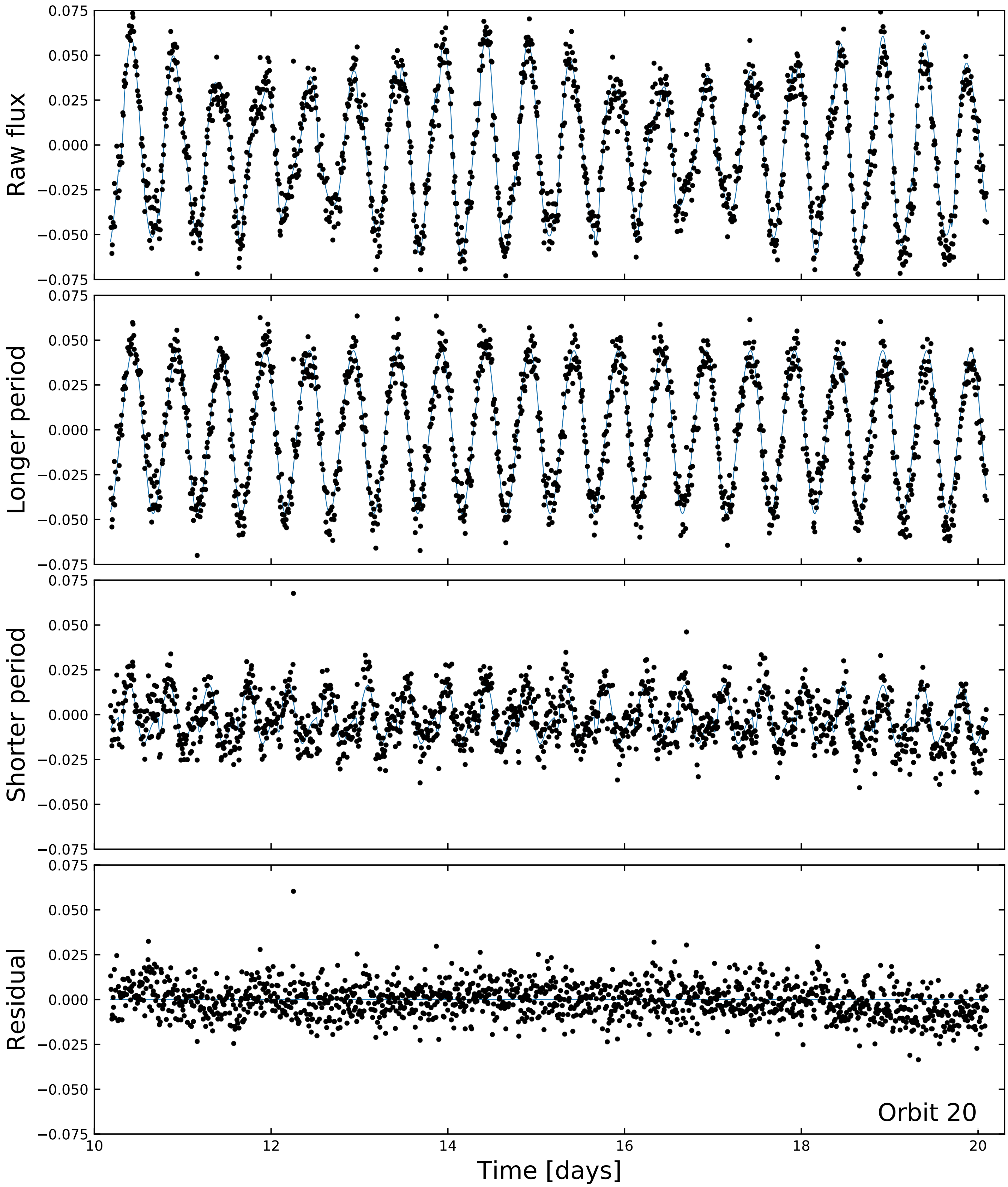

Figure 2. TESS lightcurve of PTFO 8-8695 (Sector 6, Orbit 20). Same format as Figure 1.

servations that were not strongly down-weighted in the astrometric solution. PTFO 8-8695 was assigned the Gaia DR2 identifier 3222255959210123904. Its photometric brightness was measured using selected bands (G, Rp, and Bp) of the Gaia Radial Velocity Spectrometer (Cropper et al. 2018; Evans et al. 2018). We accessed the pipeline parameters for PTFO 8-8695 using the Gaia archive[1].

The majority of Gaia's derived parameters for PTFO 8-8695 agreed with expectations from former studies (Briceño et al. 2005; van Eyken et al. 2012). The main novelty is that Gaia DR2 reported a 10.3σ "astrometric excess", indicating that the residuals to the best-fitting astrometric model were larger than expected based on the statistical uncertainties. We comment on the significance and interpretation of this excess in Section 4.

2.2.2. *Hierarchical Cluster Membership*

Gaia also provided astrometric parameters for tens of thousands of young stars in the Orion complex. Stellar populations in giant molecular cloud complexes are not monolithic; substructured groups are the norm (Briceño et al. 2007b). The Orion molecular cloud complex in particular has numerous subgroups, with ages ranging from 0.5 to 15 Myr. For an incomplete sampling, see for instance Briceño et al. (2005); Jeffries et al. (2006); Briceño et al. (2007a); Kounkel et al. (2018) and Briceño et al. (2019).

PTFO 8-8695 was initially identified as a member of the Orion OB1a sub-association and designated CVSO 30 by Briceño et al. (2005) through combined photometry and spectroscopy. Later work by Briceño et al. (2007a) clarified that PTFO 8-8695 was in a kinematically distinct subgroup of Orion OB1a, named the "25 Ori" group after its brightest member. They reported that the 25 Ori group has an isochrone age of 7–10 Myr, and a smaller fraction of stars with disks than younger nearby sub-associations (Hernández et al. 2007a).

With the Gaia astrometry, it has become clear that 25 Ori itself has distinct subgroups (Kounkel et al. 2018; Briceño et al. 2019). In describing the cluster membership of PTFO 8-8695, we follow the notation and results of Kounkel et al. (2018). These authors combined astrometric data from Gaia DR2 with near-infrared spectra from APOGEE-2 (Gunn et al. 2006; Majewski et al. 2017; Blanton et al. 2017; Zasowski et al. 2017; Cottle et al. 2018). They performed a hierarchical clustering on the six-dimensional position and velocity information to identify subgroups within the Orion complex. From smallest to largest, PTFO 8-8695 was identified as a member of the following hierarchical subgroups:

$$\text{25 Ori-1} \subset \text{25 Ori} \subset \text{Orion OB1a} \subset \text{Orion D}, \tag{1}$$

where '$\subset$' means "is a proper subset of". 25 Ori-1 is the largest subgroup of 25 Ori, with 149 identified members. Based on the color-magnitude diagram (CMD), the mean age was found to be 6.9 Myr, while the HR diagram led to an estimated age of 8.5 Myr (see Kounkel et al. 2018, Section 2.3). Kounkel et al. (2018) identified seven other smaller groups in the Orion complex near the Be star 25 Ori. These groups received higher numbers, *e.g.*, 25 Ori-2 (Age_{CMD} = 15.1 Myr; Age_{CMD} = 12.9 Myr; see also Briceño et al. 2019).

These details concerning the group membership for one object are cumbersome to those accustomed to the simple distinction between "young cluster members" and "old field stars". Although all members of the Orion complex are indeed young relative to the field, these details are essential for assessing the photometric evidence for the binarity of PTFO 8-8695, because of the degeneracy between stellar luminosity and age for pre-main-sequence stars. Having a clean sample of reference stars that are tightly associated with PTFO 8-8695 — both spatially and kinematically — minimizes contamination not only from field stars, but also from older and younger members of the Orion complex.

3. TESS ANALYSIS

3.1. *Inspection*

Our initial inspection of the TESS lightcurve, in both its 2-minute PDCSAP and 30-minute FFI forms, showed a strong sinusoidal beat signal (Figures 1 and 2, top panel). As a precursor to more detailed analysis, we calculated generalized Lomb-Scargle periodograms using `astrobase` (Lomb 1976; Scargle 1982; VanderPlas & Ivezić 2015; Bhatti et al. 2018). The two tallest peaks occur at 0.448 days and 0.499 days. We will refer to these two periods as the "shorter period" $P_{\rm s}$ and the "longer period" P_ℓ. The peak at P_ℓ is the taller of the two peaks. Lower-power harmonics of both signals are also present.

The peak-to-peak lightcurve amplitude at maximum, when the two signals interfere constructively, is about 14%. During the times of destructive interference, the peak-to-peak amplitude is about 6%. Assuming the signals are mainly sinusoidal, simple algebra tells us that the peak-to-peak amplitudes should be about 10% for the longer-period signal, and 4% for the shorter-period signal. To view the phase-folded light curves of the longer-period signal, we subtracted the best-fitting sinusoid at the shorter period; the resulting light curve appears smooth and nearly sinusoidal. But after subtracting the best-fitting sinusoid at the longer period, visual inspection of the phase-folded light curve of the shorter-period signal revealed substructure resembling the "dips" seen in previous observations. In particular, there was a $\approx$1% dip lasting about an hour. These initial impressions turned out to be consistent with the results of our more complicated analysis, described below.

3.2. *Lightcurve Model*

We fitted a model to the lightcurve consisting of a linear combination of Fourier modes with periods $P_{\rm s}$ and P_ℓ, as well as a number of harmonics chosen as described below. To try accounting for the dips, we also added an analytic transit model with period $P_{\rm s}$. Symbolically, the total flux f is given

[1] gea.esac.esa.int/archive/

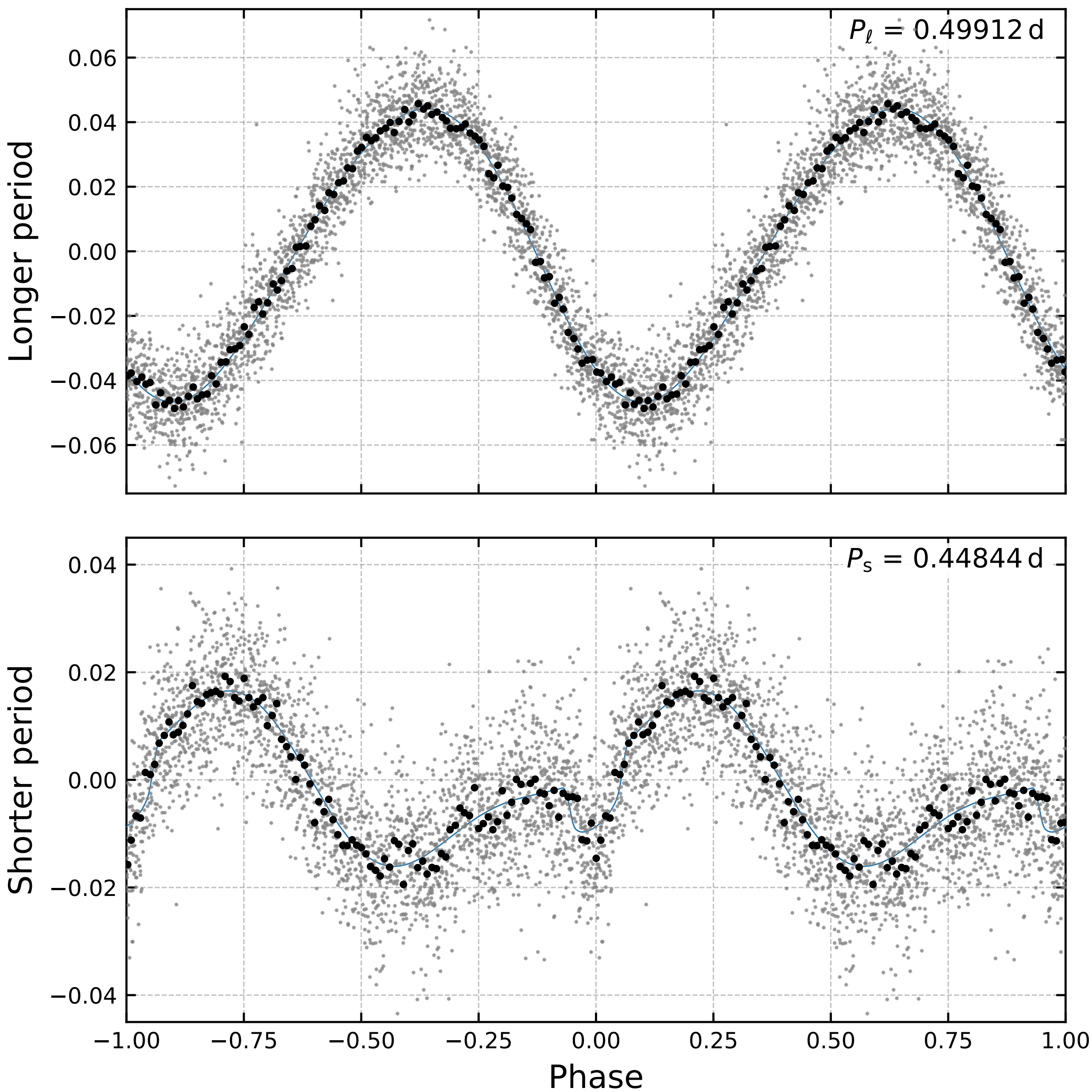

Figure 3. Phase-folded longer and shorter-period signals. *Top*: Relative flux at the longer period, as in Figure 1. *Bottom*: Relative flux at the shorter period. The reference phase is set to the dip. Gray points are the 10 minute cadence `PDCSAP` flux. Black points are binned to 100 points per period. The model (blue line) includes 2 harmonics at the longer period, plus 2 harmonics and a transit at the shorter period.

as

$$f = f_s + f_\ell = f_{\mathrm{transit,s}} + f_{\mathrm{Fourier,s}} + f_{\mathrm{Fourier},\ell}, \tag{2}$$

where f_s is the flux at the shorter period, and f_ℓ is the flux at the longer period. Writing out the Fourier terms explicitly,

$$\begin{aligned} f =& f_{\mathrm{transit,s}} + \sum_{n=1}^{N_s} A_n \sin(n\omega_s t) + \sum_{n=1}^{N_s} B_n \cos(n\omega_s t) \\ &+ \sum_{m=1}^{N_\ell} A_m \sin(m[\omega_\ell t + \phi_\ell]) + \sum_{m=1}^{N_\ell} B_m \cos(m[\omega_\ell t + \phi_\ell]), \end{aligned} \tag{3}$$

where N_s and N_ℓ are the total number of modes at the shorter and longer periods, respectively, A_i and B_i are the amplitudes of each mode (which can be positive or negative), and ω_ℓ and ω_s are the angular frequencies of the longer-period and shorter-period signals. By not including a phase parameter in the shorter-period model, we have implicitly defined the zero point of the phase scale. The relative phase of the longer-period model is specified by the phase parameter ϕ_ℓ. Since we did not know in advance how many harmonics would be appropriate to include in the model, we considered a number of different choices for N_s and N_ℓ, and used the Bayesian information criterion to select the final model (Table 1).

As an example, one possible model consists of a transit, $N_s = 2$ sines and cosines at the shorter period, plus $N_\ell = 1$ sine and cosine at the longer period. In this case, the free parameters would be as follows. The transit model parameters are the impact parameter, the planet-to-star radius ratio, two quadratic limb darkening parameters, the planet's orbital period (set equal to P_s) the time of a particular transit, and the mean flux. There would be $2N_s = 4$ additional Fourier amplitudes at the shorter period, plus $2N_\ell = 2$ Fourier amplitudes at the longer period, as well as P_ℓ itself and the relative phase ϕ_ℓ. The total number of parameters is 14.

We implemented and fitted the models using `PyMC3`, which is built on `theano` (Salvatier et al. 2016; Theano Development Team 2016). For the Fourier terms, we used the default math operators. For the exoplanet transit, we used the model and derivatives implemented in the `exoplanet` code (Foreman-Mackey et al. 2020). Our priors are listed in Table 2. To speed up the fitting process, we averaged the 2-minute lightcurve to 10-minute samples. We correspondingly scaled the uncertainties in the flux measurements by a factor of $\sqrt{5}$. Before sampling, we initialized each model with the parameters of the maximum a posteriori (MAP) model. We then assumed a Gaussian likelihood, and sampled using `PyMC3`'s gradient-based No-U-Turn Sampler (Hoffman & Gelman 2014), and used $\hat{R}$ as our convergence diagnostic (Gelman & Rubin 1992). We tested our ability to successfully recover injected parameters using synthetic data before fitting the PTFO 8-8695 lightcurves.

3.3. *Fitting Results*

We considered nine models, with the number of modes per frequency N_s and N_ℓ ranging from one to three. To select our preferred model, we used the Bayesian information criterion (Table 1). The model with the lowest BIC had two modes at the shorter 10.76 hr period, and two modes at the longer 11.98 hr period. Two other models had BIC values that provided comparable evidence (Burnham & Anderson 2016): one with ($N_s = 3$, $N_\ell = 3$), and the other with ($N_s = 3$, $N_\ell = 2$). All nine models have reduced χ^2 values ranging between 1.25 and 1.68, which suggests a plausible though imperfect agreement between the data and the model to within the formal uncertainties. Table 2 gives the best-fitting parameters for the preferred model, which has the lowest BIC value.

To explore where each model succeeded and failed, we split the raw signal into its respective components (Figures 1 and 2). We also examined the phase-folded signals (Figure 3).

In every model, the 11.98 hr variability is a simple sinusoid with peak-to-peak amplitude $\approx$10%. The 10.76 hr variability is always more complex. The overall impression is of a distorted sinusoidal function, with a peak-to-peak amplitude of about 4%. The asymmetric sinusoid rises to a maximum near phase 0.25, and reaches minimum brightness between phases −0.5 and −0.25. Between phases −0.5 and 0.0 there appears to be complex shorter-timescale variability, including an abrupt jump at phase ≈ -0.33, and ending with a "dip" of depth $\approx$1.2%, lasting $\approx$0.75 hours. The fact that the higher-order models lead to roughly comparable BIC values suggests that these sharper features may indeed be real, but that there is only weak statistical support for their existence.

The periodogram of the final residual (Figures 1 and 2 bottom row) shows a barely significant and poorly-resolved peak at $\approx$8 days, consistent with the visual impression of some slower trends in the residuals after subtracting the shorter- and longer-period signals.

4. TESTS FOR BINARITY

4.1. *Visual Binarity*

The TESS pixels are $\approx$ 21" per side. Before making any interpretations, we needed to consider whether light from neighboring stars could have contributed to the photometric signal we are attributing to PTFO 8-8695. The scene is shown in Figure 4. In the upper panels, the pixels used to measure the background level in the SPOC lightcurve are indicated with '`X`' hatching, and the pixels used in the final lightcurve aperture are shown with '`/`' hatching.

The target star, PTFO 8-8695 (TIC 264461976), has a T-band magnitude of 14.0, and its position is shown with a star. The other (unlabeled) star inside the target aperture, TIC 264461979, has $T = 16.8$ and so cannot contribute more than about 10% to the total signal. The only neighbor that is sufficiently close and bright that its light might contaminate the target star is TIC 264461980, with $T = 14.8$, which we dub "Star A". Star A is 23.6" northwest of the target, and based on the magnitude difference could contribute flux variations as large as 48% the flux of our target star, PTFO 8-8695.

The variability of PTFO 8-8695 with a period consistent with P_s had already been observed based on images with arcsecond resolution. Thus, our main concern regarding blending was whether the longer-period signal with period P_ℓ originated from PTFO 8-8695, or from Star A. We took two approaches to investigate the source of the long-period signal.

First, we examined the CDIPS FFI lightcurves of the target, which are available on MAST (Bouma et al. 2019). Three lightcurves are available, based on photometric apertures with a radius of 1, 1.5, or 2.5 pixels. The maximal peak-to-peak beat amplitude was the same to within a percent, regardless of the size of the photometric aperture that was used to create the lightcurve. If Star A were the source of the long-period variability, we would expect the peak variability amplitude to be smallest in the 1 pixel aperture, based on the separation of the sources (Figure 4, bottom). From this test alone, it seems unlikely that Star A is the source of the long-period signal.

Second, we examined the 2-minute lightcurve of each individual pixel in the scene, using the interactive tools implemented in `lightkurve` (Lightkurve Collaboration et al. 2018). If Star A were the source of the long-period variability, we would expect the pixels nearest to Star A to show a sinusoidal signal with amplitude exceeding 10%. The data do not show this pattern. The pixel directly below Star A does not clearly show any sinusoidal variability; the peak-to-peak variability in that pixel is $\lesssim$ 8%. In contrast, the south-

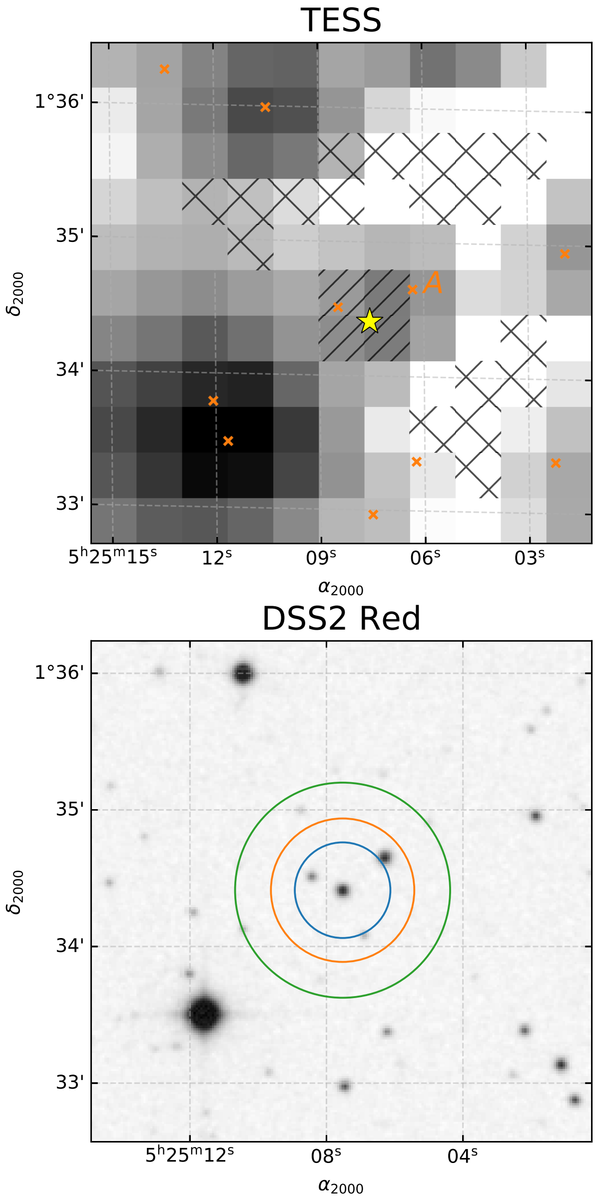

Figure 4. Scene used for blend analysis. *Top:* Mean TESS image of PTFO 8-8695 over Sector 6, with a logarithmic grayscale. The yellow star is the position of PTFO 8-8695. Orange crosses are neighboring stars with $T < 17$. The X and / hatches show the apertures used to measure the background and target star flux, respectively. *Bottom:* Digitized Sky Survey R-band image of the same field, with a linear grayscale. The circles show the apertures of radii 1, 1.5, and 2.25 pixels used in our blend analysis. To the northwest of PTFO 8-8695 and between the blue and orange circles is "Star A", the only star bright and close enough to be contributing to the signal attributed to PTFO 8-8695. However, the pixel-level TESS data showed that Star A is not the source of the observed variability (see Section 4.1).

easternmost pixel within the PTFO 8-8695 aperture (the pixel furthest from Star A that was used in the optimal aperture) shows the longer-period sinusoidal variability signal with an amplitude of 14%. We conclude that within the resolution of the Gaia DR2 source catalog, the P_s and P_ℓ signals originate from PTFO 8-8695. Based on the work of Ziegler et al. (2018), we can surmise that stellar companions with separations wider than ≈1" (349 AU) and within $\Delta G \approx 3$ magnitudes of PTFO 8-8695 would have likely been detected through this approach.

Stronger constraints on possible stellar companions were obtained by van Eyken et al. (2012) through high-resolution imaging with the NIRC2 camera on Keck II. They reported 3-σ H-band magnitude difference limits of 4.3, 6.4, and 8.9 at angular separations of 0.25, 0.5, and 1.0 arcseconds (87, 175, and 349 AU). They also detected a point source, not present in Gaia DR2, 7.0 magnitudes fainter than the target, and 1.8″ to the north-east. Due to the brightness difference, this point source[2] cannot be the source of our signals.

4.2. *Photometric Binarity*

We also used the Gaia data to see if the observed luminosity of PTFO 8-8695 is too bright to be a single star, i.e., if it is a "photometric binary." To assemble a set of stars coeval with PTFO 8-8695, we used the 25 Ori-1 members identified by Kounkel et al. (2018), and discussed in Section 2.2.2.

To define a set of non-member stars that nonetheless are subject to similar selection criteria, we defined the reference "neighborhood" as the group of at most 10^4 randomly selected non-member stars within 5 standard deviations of the mean 25 Ori-1 right ascension, declination, and parallax. We queried Gaia DR2 for these stars using `astroquery` (Ginsburg et al. 2018). This yielded 1,819 neighbors. While some of these stars may indeed be members of the Orion complex, or even of 25 Ori-1, enforcing this cut on positions and parallaxes ensures that we are comparing stars with similar amounts of interstellar reddening.

We examined the resulting five-dimensional distribution of right ascension, declination, proper motion in both directions, and parallax. The first point we noted was that 25 Ori-1 is a clearly defined over-density in each dimension: the cluster was confirmed to exist, and to be distinct from the neighborhood. PTFO 8-8695 was also within the cluster in each of these projected dimensions.

Figure 5 shows the HR diagram we constructed from the data. The diagram shows that PTFO 8-8695 is ≈0.75 magnitudes brighter than the average 25 Ori-1 star of the same color. In other words, it is about twice as bright as expected for a single star in the cluster. It also seems to be part of a "photometric binary" track that runs parallel to the main track.

The implication is that either *(i)* PTFO 8-8695 is notably younger than the kinematically identical 25 Ori-1 members, or *(ii)* PTFO 8-8695 is a binary with two components of

[2] This point source was claimed to be a potential planetary-mass object (Schmidt et al. 2016). Subsequent analysis of its colors showed that it is a background star (Lee & Chiang 2018).

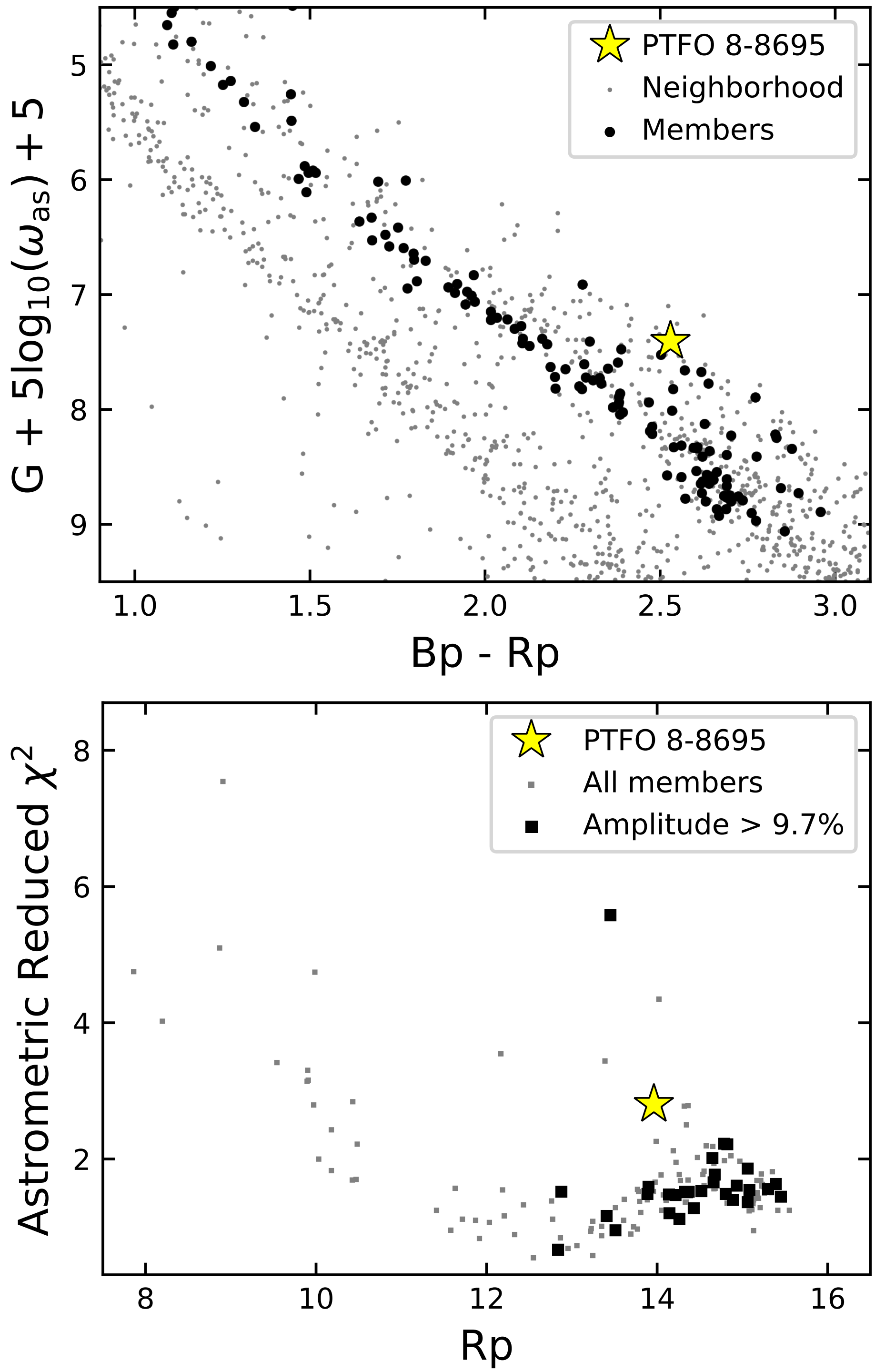

Figure 5. Evidence for binarity in PTFO 8-8695. *Top:* Hertzsprung-Russell diagram of PTFO 8-8695 and late-type members of 25 Ori-1. Members of the 25 Ori-1 group (black circles) were identified by Kounkel et al. (2018). The gray circles are stars in the "neighborhood", i.e., non-member stars within 5 standard deviations of the mean 25 Ori-1 right ascension, declination, and parallax. It contains members of the Orion complex with its full spread of ages, in addition to field interlopers. G denotes Gaia broadband magnitudes, Bp Gaia blue, Rp Gaia red, and ω_{as} the parallax in arcseconds. The x-axis limits are set to show only K and M dwarfs, to accentuate PTFO 8-8695's separation from the single-star sequence. *Bottom:* Astrometric goodness-of-fit versus Rp magnitude for 25 Ori-1 members. The single-source astrometric model for PTFO 8-8695 provides a poor fit, which could be due to stellar variability or binarity. Cluster members that are at least as variable as PTFO 8-8695 show lower astrometric excesses (black squares), suggesting binarity as the root cause.

nearly equal brightness. Since there is no other reason to suspect an age difference, and because the source showed two separate photometric signals with similar but distinct periods, the binary interpretation seems more probable.

4.3. *Astrometric Binarity*

A separate possible line of evidence for binarity is the Gaia DR2 astrometry. As noted in Section 2, the Gaia DR2 astrometric solution for PTFO 8-8695 shows a 10.3σ "astrometric excess", a parameter that quantifies the degree to which a single-star model fails to fit the astrometric measurements. Specifically, the single-source astrometric model yielded $\chi^2 = 325.2$. There are 121 astrometric measurements, and 5 free parameters, and therefore 116 degrees of freedom. The reduced χ^2 is 2.80. The majority of stars with comparable brightness in Gaia do not show such poor goodness-of-fit (see Lindegren et al. 2018, Appendix A).

Potential explanations for the poor astrometric fit include photometric variability and unresolved stellar binarity (*e.g.*, Rizzuto et al. 2018; Belokurov et al. 2020). If photometric variability were the cause, we would expect comparably faint stars in the same kinematic group of Orion to show similar astrometric excesses, as the majority of young stars are highly variable.

Using the same 149 members in the 25 Ori-1 subgroup, we calculated the astrometric reduced χ^2 for each member. We then queried the CDIPS lightcurve database at MAST (Bouma et al. 2019) to find the subset of members that were at least as variable as PTFO 8-8695. We measured the variability amplitude by taking the difference between the 95$^{\text{th}}$ and 5$^{\text{th}}$ percentiles of the flux measurements. This yielded 30 stars of equal or greater variability. The lower panel of Figure 5 shows the reduced χ^2 as a function of stellar brightness. PTFO 8-8695 is in the upper 90$^{\text{th}}$ percentile of stars showing astrometric excesses within the 25 Ori-1 group. Relative to other M-dwarf group members with comparable brightnesses and variability characteristics, PTFO 8-8695 still stands out by virtue of its failure to conform to a single-star astrometric model. This supports the interpretation that PTFO 8-8695 is a binary star.

Performing the same analysis using the renormalized unit weight error (RUWE[3]) rather than the reduced χ^2 yielded similar results. PTFO 8-8695 has a RUWE of 1.22, which corresponds to the 93$^{\text{rd}}$ percentile of 25 Ori-1 members. Two of thirty stars with variability amplitudes greater than 9.7% showed higher RUWE. One was CVSO 35, which has a TESS light-curve that varies by 2 magnitudes, and shows a strong IR excess and a 10μm silicate emission feature (Maucó et al. 2018). The other is GAIA DR2 3222210363837122048.

We will have to wait for the full release of the nominal Gaia mission to determine definitively whether the astrometric excess is caused by stellar binarity or photometric variability. Nonetheless the fact that comparably variable stars do not show comparably large astrometric excesses suggests that stellar binarity is indeed the root cause.

4.4. *Radial Velocity Binarity*

Long-baseline radial velocity (RV) measurements could also reveal the presence of multiple stars in this system. Unfortunately, the available RV data for PTFO 8-8695 is rather sparse, presumably due to the stellar faintness and equatorial velocity. The RV datasets with the longest baselines we could find in the literature were those reported by van Eyken et al. (2012). These included 5 Keck/HIRES measurements acquired over 10 days in April 2011, and 4 HET/HRS measurements acquired over 10 days in February 2011. The root-mean-squared RV over each 10 day span was $\approx 2\,\mathrm{km\,s^{-1}}$, consistent with the measurement precision. Although van Eyken et al. (2012) tried a CCF-based RV reduction technique, they eventually found that manually selecting absorption lines and measuring line centroids was more effective. While Yu et al. (2015) acquired 22 further Keck/HIRES spectra over one night in December 2013, those points were not reduced to velocities, and it is not clear whether the appropriate calibration data exist. Further Keck/HIRES measurements of PTFO 8-8695, if appropriately calibrated, could potentially confirm or refute the presence of binary companions.

5. DISCUSSION

5.1. *Longer-Period Signal*

The standard interpretation for 11.98 hr nearly sinusoidal modulations of a pre-main-sequence M dwarf is stellar rotation. This is the dominant signal in the system with 10% amplitude, and there is no evidence to suggest that this signal has any other origin.

In their report on the discovery of the unusual photometric variability, van Eyken et al. (2012) saw an alias of the longer-period signal (*e.g.*, their Figure 7), and identified it as a periodogram peak at 0.9985 ± 0.0061 days. They ascribed it to their observing cadence, because of its close correspondence to the sidereal day. Our pixel-level analysis showed that the signal is specific to only pixels near PTFO 8-8695, and no other pixels. We therefore conclude that the signal is not an artifact of systematic errors.

We are not the first to reach the conclusion that the long period sinusoidal modulation is astrophysical. A study by Koen (2015) identified the same modes and aliases as van Eyken et al. (2012), but argued that the signal was astrophysical (however they were still unsure of the exact period). Using photometry from the YETI global telescope network, Raetz et al. (2016) eventually came to the conclusion that the 0.50 d signal was indeed from stellar rotation. The TESS data strongly support this conclusion.

5.2. *Shorter-Period Signal, Including the "Dip"*

The TESS lightcurve shows a dip that lasts about 45 minutes, and seems to recur every 10.76 hours (Figures 1, 2, 3). The dip duration is roughly the same as that observed by previous investigators (van Eyken et al. 2012; Yu et al. 2015).

[3] See the Gaia DPAC technical note GAIA-C3-TN-LU-LL-124-01, http://www.rssd.esa.int/doc_fetch.php?id=3757412, accessed 2020-04-27.

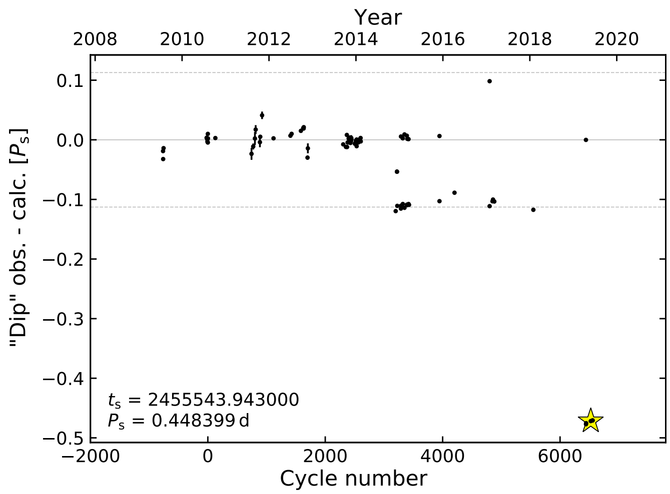

Figure 6. Timing residuals for PTFO 8-8695b based on a decade of monitoring. Black points are times of dips, minus the indicated linear ephemeris. The phase of the shorter-period signal is plotted on the y-axis. The star symbol represents the TESS ephemeris. Dips were observed by van Eyken et al. (2012), Ciardi et al. (2015), Yu et al. (2015), Raetz et al. (2016), Onitsuka et al. (2017), and Tanimoto et al. (2020). Certain dips (*e.g.*, the one at phase 0 in mid-2019) are consistent with noise, and were likely reported because dips were expected, rather than convincingly observed. Horizontal dashed lines are drawn at $\pm(P_\ell - P_s)/P_s$, highlighting either a numerical coincidence or an observational bias. The orbital phase observed by TESS (lower-right) is consistent with that of Tanimoto et al. (2020).

The 1.2% depth is similar to what has been observed in the near-infrared (Onitsuka et al. 2017). However the dip depth seems likely to have evolved over time between being not present at all, to a maximum of ≈5% (*e.g.*, Koen 2015; Yu et al. 2015; Tanimoto et al. 2020).

One particularly interesting feature of the dip is its epoch. The dips do not occur with strict periodicity (Yu et al. 2015). In fact, Tanimoto et al. (2020) provided stark evidence for different behavior altogether: over a time-span of years, the dip “split” into distinct groups at particular repeating phases. See for instance their Figures 2 through 4. Fitting a decade of observations, they provided the following linear ephemeris, which we did not find any need to update.

$$t_0 \ \mathrm{BJD_{TDB}} = 2455543.943 \pm 0.002 \quad (4)$$
$$P = 0.4483993 \pm 0.0000006d. \quad (5)$$

Figure 6 shows the phase of the dip we detected in the TESS data, relative to their ephemeris. It agrees with the independent December 2018 measurements by Tanimoto et al. (2020): either the dip abruptly shifted phase over the past decade or, more likely, there are multiple dips that have come and gone at different phases.

Figure 6 shows two additional strange features: *(i)* multiple dips per cycle, and *(ii)* a set of dips numerically coincident with phase $(P_\ell - P_s)/P_s$. The observation of multiple dips per cycle in 2015 was seen independently by both Yu et al. (2015) and Tanimoto et al. (2020). It therefore seems credible. Inspecting the Tanimoto et al. (2020) lightcurves, the claim of multiple dips per cycle in December 2018 at phase 0 and −0.47 seems less plausible—the phase -0.47 dips are strongly detected, while the suggested phase 0 dip is not clearly present in the data.

We are not sure what to make of the numerical coincidence. The ratio of long to short periods is roughly 10:9. It is not clear that this would obviously translate into an observational bias unless by some fluke three season’s worth of observations managed to only observe every ninth dip. This is of course not the case, and we therefore leave this curiosity as observation *sans* interpretation.

5.3. *Short Period Out-of-Dip Modulation*

Visually, the out-of-dip modulation at the 10.76 hr period resembles a slightly asymmetric sinusoid (Figure 3). Non-zero contributions in both the first and second harmonics are detected (Table 2). The first sine and cosine harmonic both have amplitudes of roughly $0.9 \pm 0.1\%$. The second sine harmonic has amplitude $0.16 \pm 0.07\%$, so is non-zero at a significance of only 2.3σ. The second cosine harmonic has negative amplitude $0.53 \pm 0.06\%$. In our sign convention, the fact that it is negative means that this component peaks at phase 0.25 and 0.75.

5.3.1. *Ellipsoidal Variability?*

If there were a giant planet transiting PTFO 8-8695, it would tidally distort the host star, and cause ellipsoidal photometric modulations that also peak at quadrature (see Shporer 2017). Interpreting the second cosine harmonic as planet-induced tidal distortion, it would imply a minimum planet mass $M_p \sin i$ of $3.8 M_{\rm Jup}$. For this estimate, we assumed $R_\star = 1.39 R_\odot$, and $M_\star = 0.39 M_\odot$ (van Eyken et al. 2012). This ellipsoidal amplitude is larger than the typical modulations induced by close-in giant planets because the host star is puffy, and still on the pre-main-sequence.

The planetary interpretation however does not readily explain the first sine and cosine harmonics. Interpreting the sine component as Doppler beaming would imply a secondary mass greater than the primary ($0.86 M_\odot$). Interpreting the cosine component as reflected or emitted light from the planet’s surface is nonsensical because the sign is wrong—the planet would need to be *absorbing* light.

5.3.2. *Similar Lightcurves*

When physical explanations are not forthcoming, taxonomy is a useful exercise. By searching the literature, we have found about a dozen lightcurves with similar morphologies to PTFO 8-8695, drawn from surveys of low-mass weak-lined T Tauri stars in regions including ρ Oph, Upper Sco, Taurus, and perhaps the Pleiades (Rebull et al. 2016; David et al. 2017; Stauffer et al. 2017, 2018; Rebull et al. 2018, 2020). These surveys were performed using K2 (Howell et al. 2014). We downloaded some of these lightcurves from MAST, opt-

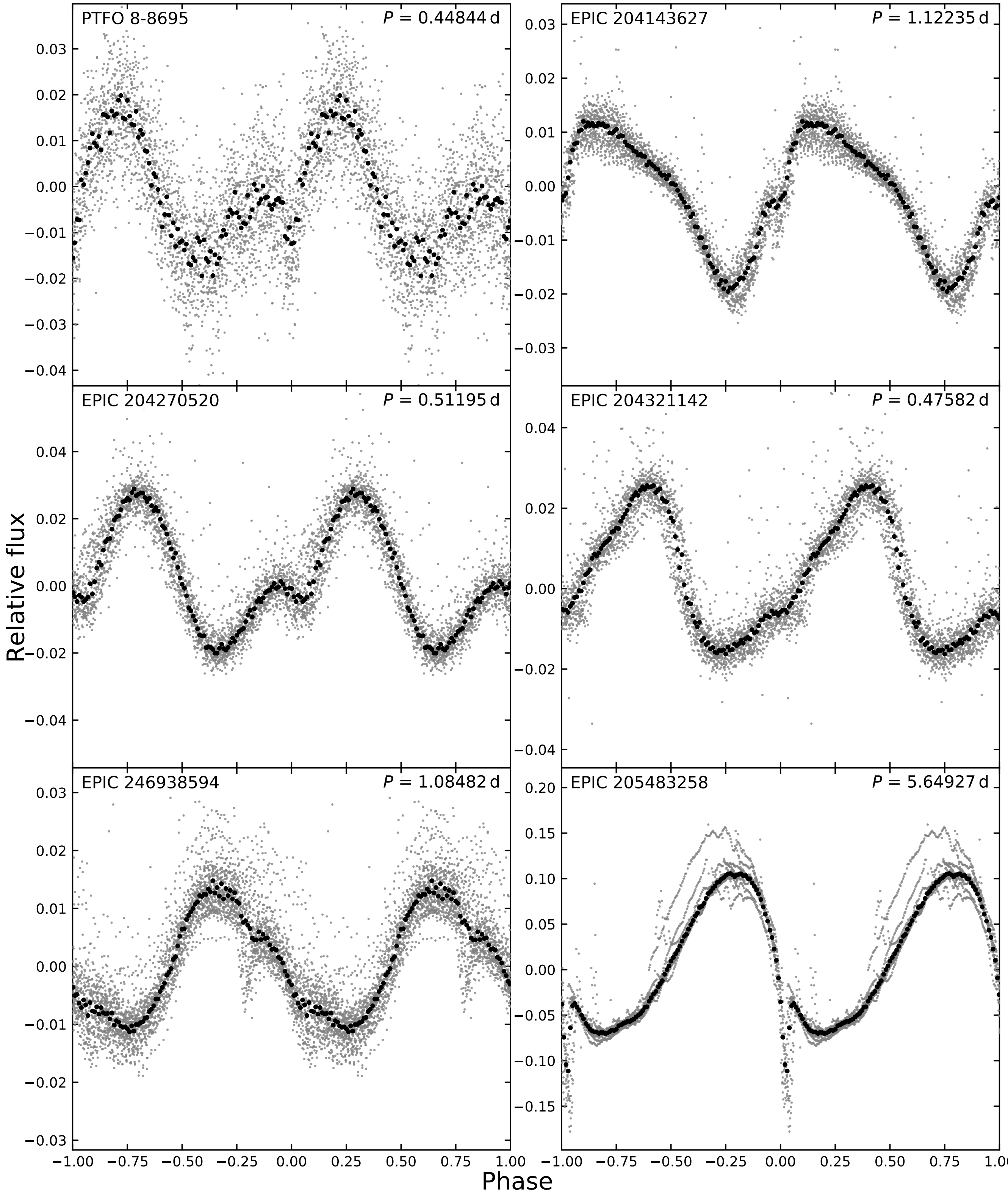

Figure 7. PTFO 8-8695 and its brethren. Five transient and persistent flux dip stars selected based on their visual similarity to the short-period signal in PTFO 8-8695 are as shown. They include EPIC 204143627, EPIC 204270520, EPIC 204321142, EPIC 246938594, and EPIC 205483258 (RIK-210). RIK-210 has the longest period of any of these objects. All the analogs displayed are either in Taurus or Upper Sco, and meet the characteristics of Section 5.3.2. We found these objects through studies by Stauffer et al. (2017), David et al. (2017), and Rebull et al. (2018).

ing for the EVEREST reductions (Luger et al. 2016, 2018). They are plotted in Figure 7.

These lightcurves have been phenomenologically classified as "persistent flux dips" or "transient flux dips", based on whether their depths and durations show variability over the 90-day K2 campaigns (Stauffer et al. 2017). In the terminology of Stauffer et al. (2017), these objects are morphologically distinct from "scallop shell" lightcurves, and are present in stars at more advanced evolutionary disk stages than the "dipper" stars (Ansdell et al. 2016; Cody & Hillenbrand 2018). The persistent and transient flux dip stars all show angular dips that are cannot be explained as the effects of starspots. These stars typically have the following things in common:

1. They are weak-lined T Tauri stars.
2. The spectral type is M2 to M5 (*e.g.*, Rebull et al. 2018, Figure 20).
3. The age is typically[4] $\lesssim 100$ Myr.
4. The lightcurves show shallow, angular dips, usually superposed on large-amplitude smooth variability. The latter is interpreted as stellar rotation.
5. The rotation is rapid—usually between 0.5 and 2.0 days.
6. There is rarely any detectable infrared excess in WISE data (never any W4 detection; only a few W3 detections).
7. They sometimes show multiple dips per cycle.
8. The dip depths, durations, and phases can vary over just a few cycles (*e.g.*, EPIC 204143627).
9. The dip depths can change after flares.
10. They are rare at a population level: $\lesssim 1\%$ of relevant stars (Rebull et al. 2018).

The 10.76 hr signal in PTFO 8-8695 meets all of these criteria. This is the first connection of PTFO 8-8695 with this class of objects because the TESS lightcurve was needed to resolve the different rotation signals.

There are two crucial additional points concerning the transient flux dips. First, the dip durations seem to scale linearly with the photometric periods (Stauffer et al. 2017, Figure 26). In the usual idealized limits, the transit duration T of a point source across the stellar disk scales as $T \propto R_\star (P/M_\star)^{1/3}$ (Winn 2010). While the shortest period $\approx$0.5-day transient flux dip stars have dip durations consistent with point sources, at longer periods of 1 to 5 days the dip durations become many hours, far too long to be caused by planetary transits.

Second, between 40-50% of the transient flux dip stars discovered in ρ Oph and Upper Sco show two Lomb-Scargle periods, and so are apparently binaries (Stauffer et al. 2017, Table 1). This is higher than the main-sequence companion fraction of $\mathrm{CF}^{\mathrm{MS}}_{0.1\text{-}0.5\,M_\odot} = 33 \pm 5\%$ (Henry et al. 2006; Duchêne & Kraus 2013; Winters et al. 2019). Low-mass pre-main-sequence stars however have been shown to companion fractions up to twice as high in dispersed clusters such as Upper Sco and Taurus (Kraus et al. 2008, 2011). A detailed high-resolution imaging survey would be necessary to determine whether the transient flux dip stars truly have any distinct population-level binarity properties relative to other young low-mass stars.

5.4. *Physical Interpretation*

The evidence for binarity in PTFO 8-8695 is as follows. First, the star is photometrically twice as bright as stars of the same color in its kinematic group (Figure 5). Second, it shows two distinct photometric signals. These points alone suggest binarity (Stauffer et al. 2018). For the case of PTFO 8-8695, there is a third line of evidence: the Gaia DR2 entry for PTFO 8-8695 reports a poor fit of the single-star model to the astrometric data. While this could be caused by stellar variability, other cluster members that are just as variable do not typically show the same level of excess astrometric motion. Therefore the astrometric excess is a suggestive third line of evidence for binarity in PTFO 8-8695. To us, the evidence leads to the conclusion that PTFO 8-8695 is a nearly equal-mass binary consisting of two rapidly rotating stars.

Based on the lack of an infrared excess seen by Yu et al. (2015), the primordial gas disks seem to be have been depleted[5] around both stars in PTFO 8-8695. The stars are therefore no longer magnetically locked to their disks. This is consistent with the $\approx$half-day periodicities of both rotation signals: young disked M dwarfs typically rotate with periods of two days or more due to magnetic locking (*e.g.*, Rebull et al. 2020). If the two stars are within $\approx$50 AU of each other, as required by the NIRC2 adaptive optics imaging, then it would also be expected that the stars would truncate the outer edges of their respective disks, in a manner seen at the population level in exoplanetary systems (Kraus et al. 2016; Moe & Kratter 2019). This hard outer boundary condition could propagate to the inner disk and affect its evolution.

The main physical question is what causes the transient dips. This is an unsolved problem not only for PTFO 8-8695 but also for an emerging class of similar young rapidly rotating M-dwarfs. Many possible explanations have been detailed by Rebull et al. (2016), David et al. (2017), Stauffer et al. (2017), and Zhan et al. (2019). Their disfavored explanations include that the dips are caused by *(i)* eclipsing binaries; *(ii)* "dipper"-flavor Class-I or Class-II disks; *(iii)* eclipses of prominences; *(iv)* high-latitude accretion hotspots; *(v)* high-latitude starspots; or *(vi)* dust clouds of plausible composition. We also view the possibility of *(vii)*

[4] At present, the oldest observed "scallops" are in the Pleiades (Rebull et al. 2016). One of these, EPIC 211013604, might meet the "persistent dip" classification. If so, it is also the oldest known.

[5] A potential confounding factor is completeness. Is Spitzer sensitive to infrared excesses at the distance of Orion? The series of studies by Hernández et al. (2006, 2007a,b, 2009) show that it is.

tidally disrupted planetary or cometary material to be implausible, given the synchronicity between dip and rotation periods seen across many systems.

The explanations that are not yet ruled out include *(i)* transiting clumps of gas at the Keplerian corotation radius; *(ii)* transits of enshrouded protoplanets; *(iii)* occultations of starspots by an optically thick disk. The first and last explanations have added appeal because they are flexible enough to explain not only the transient and persistent-dip M-dwarfs, but also the "scallop shell" M-dwarfs (Stauffer et al. 2017). Despite this appeal, the possibility of distinct mechanisms explaining these distinct variability classes remains open.

The evolution of PTFO 8-8695 over the past decade (Figure 6) could offer important hints. Specifically, PTFO 8-8695's transition between having none, one, and multiple dips per cycle seems important. It strains the "enshrouded protoplanet" interpretation, because there are no known processes that cause a planet's orbital phase to jump. The dips would then need to be caused by material that was somehow disrupted from the planet, but somehow remained co-orbital for an extended duration. This seems implausible.

6. CONCLUSIONS

The combination of TESS and Gaia data has clarified a few things about the PTFO 8-8695 system. Our main results are as follows.

- *The TESS light-curve shows two periodic signals.* The "long" signal is a 10% peak-to-peak sinusoid that repeats every 11.98 hours. The "short" signal is a 4% peak-to-peak "dip + asymmetric sinusoid" that repeats every 10.76 hours. The signals beat, and therefore cannot be an artifact linked to data processing. Within the angular resolution of the Gaia source catalog, both signals need to originate from PTFO 8-8695.

- *The Gaia data imply binarity.* Relative to stars in its kinematic group, PTFO 8-8695 is a photometric binary (Figure 5, top). Relative to stars in its group that are at least as photometrically variable, PTFO 8-8695 also shows signs of astrometric binarity (Figure 5, bottom).

- *The orbital phase of the dip has changed since the discovery by van Eyken et al. (2012).* As shown in Figure 6, the phase seems to have jumped, perhaps twice. This agrees with the recent study by Tanimoto et al. (2020).

- *All properties of PTFO 8-8695 are consistent with the emerging class of transient and persistent flux dip stars.* Analogous lightcurves are shown in Figure 7. Properties of this variability class are enumerated in Section 5.3.2.

The physical mechanism that explains the transient and persistent flux dips is unresolved. Our preferred explanations include transiting clumps of gas at the Keplerian corotation radius, and occultations of starspots by an optically thick disk (*e.g.*, Stauffer et al. 2017; David et al. 2017; Zhan et al. 2019). The jumping orbital phase disfavors the explanation of an enshrouded, transiting protoplanet. Though PTFO 8-8695b may not be a planet, as we and others had hoped, understanding PTFO 8-8695 and its analogs is a worthy problem that might even teach us about the natal environments of the majority of habitable-zone Earth-sized planets in the Milky Way (Dressing & Charbonneau 2013).

When this manuscript was at an advanced stage, we learned of the complementary work by Koen (2020), which was in press at the *Monthly Notices* before submission of our manuscript. Our studies independently reached the key conclusions that the TESS lightcurve shows two periodic signals, and that the properties of PTFO 8-8695 are consistent with the emerging class of transient and persistent flux dip stars. Koen (2020) reached these conclusions by modeling the TESS lightcurve as a truncated sum of Fourier terms, and concluded that the two signals are most simply interpreted as coming from two stars. Our analysis of the Gaia data provide independent support for the conclusion that PTFO 8-8695 is a binary.

Minor differences in our approaches are that Koen (2020) interprets the "out of dip" signal to potentially show multiple dips, while our BIC-based model comparison did not indicate that including additional harmonics past the second order was strictly necessary (Table 1). Our analysis emphasized the agreement between the TESS dip ephemeris and that from Tanimoto et al. (2020). Koen (2020) however made a clearer case for testing the binarity hypothesis using interferometric imaging and high-precision radial velocities.

The authors thank D. Fabrycky, S. Mahadevan, G. Stefánsson, and A. Vanderburg for helpful calculations, observations, and suggestions. We also thank the Heising-Simons Foundation for their generous support of this work. PTFO 8-8695 was included on the TESS "short-cadence" target list thanks to the Guest Investigator programs of S. Czesla and C. Huang (G011128 and G011132 respectively). The Digitized Sky Survey was produced at the Space Telescope Science Institute under U.S. Government grant NAG W-2166. Figure 4 is based on photographic data obtained using the Oschin Schmidt Telescope on Palomar Mountain.

Software: `astrobase` (Bhatti et al. 2018), `astropy` (Astropy Collaboration et al. 2018), `astroquery` (Ginsburg et al. 2018), `cdips-pipeline` (Bhatti et al. 2019) `corner` (Foreman-Mackey 2016), `exoplanet` (Agol et al. 2019) `exoplanet` (Foreman-Mackey et al. 2020), and its dependencies (Agol et al. 2019; Kipping 2013; Luger et al. 2019; Theano Development Team 2016). `IPython` (Pérez & Granger 2007), `lightkurve` (Lightkurve Collaboration et al. 2018), `matplotlib` (Hunter 2007), `MESA` (Paxton et al. 2011, 2013, 2015) `numpy` (Walt et al. 2011), `pandas` (McKinney 2010), `pyGAM` (Servén et al. 2018), `PyMC3` (Salvatier et al. 2016), `scipy` (Jones et al. 2001). `tesscut` (Brasseur et al. 2019), `wotan` (Hippke et al. 2019).

Facilities: *Astrometry*: Gaia (Gaia Collaboration et al. 2016, 2018). *Imaging*: Second Generation Digitized Sky Survey, Keck:II (NIRC2; www2.keck.hawaii.edu/inst/nirc2). *Spectroscopy*: Keck:I (HIRES; Vogt et al. 1994). *Photometry*: TESS (Ricker et al. 2015).

Table 1. Model Comparison.

Description	N_s	N_ℓ	N_{data}	N_{param}	χ^2	χ^2_{red}	BIC	ΔBIC
Favored	2	2	2585	17	3230.2	1.258	3363.7	0.0
Weakly favored	3	3	2585	21	3203.4	1.249	3368.4	4.7
—	3	2	2585	19	3222.9	1.256	3372.2	8.4
Disfavored	2	3	2585	19	3244.9	1.265	3394.2	30.4
—	2	1	2585	15	3410.6	1.327	3528.5	164.7
—	3	1	2585	17	3396.4	1.323	3530.0	166.3
—	1	2	2585	15	4158.6	1.618	4276.4	912.7
—	1	3	2585	17	4147.4	1.615	4281.0	917.2
—	1	1	2585	13	4313.5	1.677	4415.6	1051.9

NOTE— N_s and N_ℓ are the number of harmonics at the short and long periods, respectively. N_{data} is the number of fitted flux measurements. N_{param} is the number of free parameters in the model. The Bayesian information criterion (BIC) and the difference from the maximum ΔBIC are also listed.

Table 2. Best-fit model priors and posteriors.

Param.	Prior	Mean	Std. Dev.	3rd Pct.	97th Pct.
P_s	$\mathcal{N}(0.4485; 0.0010)$	0.4484592	0.0000448	0.4483738	0.4485432
$t_s^{(1)}$	$\mathcal{N}(0.438096; 0.0020)$	0.438964	0.0011541	0.4367218	0.4410819
$R_p/R_\star$	$\mathcal{N}(0.1100; 0.0110)$	0.11461	0.00588	0.10407	0.12581
b	$\mathcal{U}(0; 1+R_p/R_\star)$	0.8103	0.0430	0.7279	0.8831
u_1	(2)	0.634	0.463	0.	1.492
u_2	(2)	0.033	0.404	-0.736	0.779
Mean	$\mathcal{U}(-0.01; 0.01)$	-0.000924	0.000195	-0.001275	-0.000539
ω_s	$2\pi/P_s$	14.01061	0.00140	14.00798	14.01327
$A_{s,0}$	$\mathcal{U}(-0.02; 0.02)$	0.009025	0.000383	0.008243	0.009695
$B_{s,0}$	$\mathcal{U}(-0.02; 0.02)$	0.009843	0.000383	0.009152	0.010563
$A_{s,1}$	$\mathcal{U}(-0.02; 0.02)$	0.001571	0.000337	0.000951	0.002223
$B_{s,1}$	$\mathcal{U}(-0.02; 0.02)$	-0.005324	0.000282	-0.005866	-0.004791
ϕ_ℓ	$\mathcal{U}(1.3721; 2.1575)$	1.75981	0.20755	1.40468	2.07790
ω_ℓ	$\mathcal{N}(12.6054; 0.1261)$	12.588617	0.000907	12.586906	12.590249

Table 2 continued

Table 2 *(continued)*

Param.	Prior	Mean	Std. Dev.	3rd Pct.	97th Pct.
$A_{\ell,0}$	$\mathcal{U}(-0.06; 0.06)$	0.038302	0.004652	0.030051	0.044614
$B_{\ell,0}$	$\mathcal{U}(-0.06; 0.06)$	0.021721	0.008029	0.008567	0.034349
$A_{\ell,1}$	$\mathcal{U}(-0.02; 0.02)$	0.002271	0.000535	0.001288	0.003178
$B_{\ell,1}$	$\mathcal{U}(-0.02; 0.02)$	-0.00222	0.000539	-0.00309	-0.001201

Note that $R_p/R_\star$ is post-correction for the dilution by Star A and other neighboring stars, according to the PDCSAP lightcurve's `CROWDSAP` value in the optimal aperture of 0.73. (1) To convert mean TESS mid-transit time to BJD_{TDB}, add 2458468.2. (2) Quadratic limb-darkening prior from Kipping (2013), implemented by Foreman-Mackey et al. (2020).

REFERENCES

Agol, E., Luger, R., & Foreman-Mackey, D. 2019, arXiv e-prints, 1908.03222

Ansdell, M., Gaidos, E., Rappaport, S. A., et al. 2016, ApJ, 816, 69

Astropy Collaboration, Price-Whelan, A. M., Sipőcz, B. M., et al. 2018, AJ, 156, 123

Barnes, J. W., van Eyken, J. C., Jackson, B. K., Ciardi, D. R., & Fortney, J. J. 2013, ApJ, 774, 53

Belokurov, V., Penoyre, Z., Oh, S., et al. 2020, arXiv:2003.05467 [astro-ph], arXiv: 2003.05467

Bhatti, W., Bouma, L., & Yee, S. 2019, `cdips-pipeline v0.1.0`, https://doi.org/10.5281/zenodo.3370324

Bhatti, W., Bouma, L. G., & Wallace, J. 2018, `astrobase`, https://doi.org/10.5281/zenodo.1469822

Blanton, M. R., Bershady, M. A., Abolfathi, B., et al. 2017, AJ, 154, 28

Bouma, L. G., Hartman, J. D., Bhatti, W., Winn, J. N., & Bakos, G. Á. 2019, ApJS, 245, 13

Brasseur, C. E., Phillip, C., Fleming, S. W., Mullally, S. E., & White, R. L. 2019, Astrophysics Source Code Library, ascl:1905.007

Briceño, C., Calvet, N., Hernández, J., et al. 2005, AJ, 129, 907

Briceño, C., Hartmann, L., Hernández, J., et al. 2007a, ApJ, 661, 1119

Briceño, C., Preibisch, T., Sherry, W. H., et al. 2007b, Protostars and Planets V, 345

Briceño, C., Calvet, N., Hernández, J., et al. 2019, AJ, 157, 85

Burnham, K. P., & Anderson, D. R. 2016, Sociological Methods & Research

Ciardi, D. R., Eyken, J. C. v., Barnes, J. W., et al. 2015, ApJ, 809, 42, publisher: IOP Publishing

Cody, A. M., & Hillenbrand, L. A. 2018, AJ, 156, 71

Cottle, J., Covey, K. R., Suárez, G., et al. 2018, ApJS, 236, 27

Cropper, M., Katz, D., Sartoretti, P., et al. 2018, A&A, 616, A5

David, T. J., Petigura, E. A., Hillenbrand, L. A., et al. 2017, ApJ, 835, 168

Dressing, C. D., & Charbonneau, D. 2013, ApJ, 767, 95

Duchêne, G., & Kraus, A. 2013, ARA&A, 51, 269

Evans, D. W., Riello, M., De Angeli, F., et al. 2018, A&A, 616, A4

Foreman-Mackey, D. 2016, The Journal of Open Source Software, 24

Foreman-Mackey, D., Czekala, I., Luger, R., et al. 2020, exoplanet-dev/exoplanet v0.2.6

Gaia Collaboration, Prusti, T., de Bruijne, J. H. J., et al. 2016, A&A, 595, A1

Gaia Collaboration, Brown, A. G. A., Vallenari, A., et al. 2018, A&A, 616, A1

Gelman, A., & Rubin, D. B. 1992, Statistical Science, 7, 457, publisher: Institute of Mathematical Statistics

Ginsburg, A., Sipocz, B., Madhura Parikh, et al. 2018, Astropy/Astroquery: V0.3.7 Release

Gunn, J. E., Siegmund, W. A., Mannery, E. J., et al. 2006, AJ, 131, 2332

Henry, T. J., Jao, W.-C., Subasavage, J. P., et al. 2006, AJ, 132, 2360

Hernández, J., Briceño, C., Calvet, N., et al. 2006, ApJ, 652, 472

Hernández, J., Calvet, N., Hartmann, L., et al. 2009, ApJ, 707, 705

Hernández, J., Calvet, N., Briceño, C., et al. 2007a, ApJ, 671, 1784

Hernández, J., Hartmann, L., Megeath, T., et al. 2007b, ApJ, 662, 1067

Hippke, M., David, T. J., Mulders, G. D., & Heller, R. 2019, arXiv:1906.00966 [astro-ph], arXiv: 1906.00966

Hoffman, M. D., & Gelman, A. 2014, Journal of Machine Learning Research, 15, 1593

Howarth, I. D. 2016, MNRAS, 457, 3769

Howell, S. B., Sobeck, C., Haas, M., et al. 2014, PASP, 126, 398

Hunter, J. D. 2007, Computing in Science & Engineering, 9, 90

Jeffries, R. D., Maxted, P. F. L., Oliveira, J. M., & Naylor, T. 2006, MNRAS, 371, L6
Jenkins, J. M., Twicken, J. D., McCauliff, S., et al. 2016, Software and Cyberinfrastructure for Astronomy IV, 9913, 99133E
Johns-Krull, C. M., Prato, L., McLane, J. N., et al. 2016, ApJ, 830, 15
Jones, E., Oliphant, T., Peterson, P., et al. 2001, Open source scientific tools for Python
Kamiaka, S., Masuda, K., Xue, Y., et al. 2015, Publications of the Astronomical Society of Japan, 67, 94
Kipping, D. M. 2013, MNRAS, 435, 2152
Koen, C. 2015, MNRAS, 450, 3991
Koen, C. 2020, MNRAS
Kounkel, M., Covey, K., Suárez, G., et al. 2018, AJ, 156, 84
Kraus, A. L., Ireland, M. J., Huber, D., Mann, A. W., & Dupuy, T. J. 2016, AJ, 152, 8
Kraus, A. L., Ireland, M. J., Martinache, F., & Hillenbrand, L. A. 2011, ApJ, 731, 8
Kraus, A. L., Ireland, M. J., Martinache, F., & Lloyd, J. P. 2008, ApJ, 679, 762
Lee, C.-H., & Chiang, P.-S. 2018, ApJL, 852, L24
Lightkurve Collaboration, Cardoso, J. V. d. M., Hedges, C., et al. 2018, Lightkurve: Kepler and TESS time series analysis in Python, Astrophysics Source Code Library, ascl:1812.013
Lindegren, L., Hernández, J., Bombrun, A., et al. 2018, Astronomy & Astrophysics, 616, A2
Lomb, N. R. 1976, Astrophysics and Space Science, 39, 447
Luger, R., Agol, E., Foreman-Mackey, D., et al. 2019, AJ, 157, 64
Luger, R., Agol, E., Kruse, E., et al. 2016, AJ, 152, 100
Luger, R., Kruse, E., Foreman-Mackey, D., Agol, E., & Saunders, N. 2018, AJ, 156, 99
Majewski, S. R., Schiavon, R. P., Frinchaboy, P. M., et al. 2017, AJ, 154, 94
Maucó, K., Briceño, C., Calvet, N., et al. 2018, The Astrophysical Journal, 859, 1
McKinney, W. 2010, in Proceedings of the 9th Python in Science Conference, ed. S. van der Walt & J. Millman, 51
Moe, M., & Kratter, K. M. 2019, arXiv:1912.01699 [astro-ph], arXiv: 1912.01699
Onitsuka, M., Fukui, A., Narita, N., et al. 2017, Publications of the Astronomical Society of Japan, 69
Paxton, B., Bildsten, L., Dotter, A., et al. 2011, ApJS, 192, 3
Paxton, B., Cantiello, M., Arras, P., et al. 2013, ApJS, 208, 4
Paxton, B., Marchant, P., Schwab, J., et al. 2015, ApJS, 220, 15
Pérez, F., & Granger, B. E. 2007, Computing in Science and Engineering, 9, 21
Raetz, S., Schmidt, T. O. B., Czesla, S., et al. 2016, MNRAS, 460, 2834
Rebull, L. M., Stauffer, J. R., Cody, A. M., et al. 2020
—. 2018, AJ, 155, 196
Rebull, L. M., Stauffer, J. R., Bouvier, J., et al. 2016, AJ, 152, 114
Ricker, G. R., Winn, J. N., Vanderspek, R., et al. 2015, Journal of Astronomical Telescopes, Instruments, and Systems, 1, 014003
Rizzuto, A. C., Vanderburg, A., Mann, A. W., et al. 2018, arXiv:1808.07068 [astro-ph], arXiv: 1808.07068
Salvatier, J., Wieckiâ, T. V., & Fonnesbeck, C. 2016, PyMC3: Python probabilistic programming framework
Scargle, J. D. 1982, ApJ, 263, 835
Schmidt, T. O. B., Neuhäuser, R., Briceño, C., et al. 2016, A&A, 593, A75
Servén, D., Brummitt, C., & Abedi, H. 2018, dswah/pyGAM: v0.8.0
Shporer, A. 2017, PASP, 129, 072001
Smith, J. C., Morris, R. L., Jenkins, J. M., et al. 2016, PASP, 128, 124501
Smith, J. C., Stumpe, M. C., Cleve, J. E. V., et al. 2012, PASP, 124, 1000
Stassun, K. G., Oelkers, R. J., Pepper, J., et al. 2018, AJ, 156, 102
Stassun, K. G., Oelkers, R. J., Paegert, M., et al. 2019, arXiv:1905.10694 [astro-ph], arXiv: 1905.10694
Stauffer, J., Rebull, L. M., Cody, A. M., et al. 2018, AJ, 156, 275, publisher: American Astronomical Society
Stauffer, J., Cameron, A. C., Jardine, M., et al. 2017, AJ, 153, 152
Stumpe, M. C., Smith, J. C., Catanzarite, J. H., et al. 2014, PASP, 126, 100
Tanimoto, Y., Yamashita, T., Ui, T., et al. 2020, PASJ, arXiv:2001.00148 [astro-ph.EP]
Tenenbaum, P., & Jenkins, J. 2018, TESS Science Data Products Description Document, EXP-TESS-ARC-ICD-0014 Rev D, https://archive.stsci.edu/missions/tess/doc/EXP-TESS-ARC-ICD-TM-0014.pdf
Theano Development Team. 2016, arXiv e-prints, abs/1605.02688
van Eyken, J. C., Ciardi, D. R., von Braun, K., et al. 2012, ApJ, 755, 42
VanderPlas, J. T., & Ivezić, Z. 2015, ApJ, 812, 18
Vogt, S. S., Allen, S. L., Bigelow, B. C., et al. 1994, SPIE Conference Series, ed. D. L. Crawford & E. R. Craine, Vol. 2198
Walt, S. v. d., Colbert, S. C., & Varoquaux, G. 2011, Computing in Science & Engineering, 13, 22
Winn, J. N. 2010, Exoplanet Transits and Occultations, ed. S. Seager, 55
Winters, J. G., Henry, T. J., Jao, W.-C., et al. 2019, The Astronomical Journal, 157, 216
Yu, L., Winn, J. N., Gillon, M., et al. 2015, ApJ, 812, 48
Zasowski, G., Cohen, R. E., Chojnowski, S. D., et al. 2017, AJ, 154, 198
Zhan, Z., Günther, M. N., Rappaport, S., et al. 2019, ApJ, 876, 127
Ziegler, C., Law, N. M., Baranec, C., et al. 2018, arXiv:1806.10142 [astro-ph], arXiv: 1806.10142